Ultra-transient grating spectroscopy for visualization of surface acoustics

Tomáš Grabec[1], **Pavla Stoklasová**[1], **Kristýna Repček**[1], **Jakub Kušnír**[1,2], **David Mareš**[1], **Martin Ševčík**[1], **Petr Sedlák**[1], **and Hanuš Seiner**[1,*]

[1]Institute of Thermomechanics, Czech Academy of Science, Dolejskova 1402/5, 182 00 Prague, Czechia
[2]Faculty of Nuclear Science and Physical Engineering, Czech Technical University in Prague, Trojanova 13, 120 00 Prague, Czechia
[*]**Corresponding author:** hseiner@it.cas.cz (H. Seiner)

Abstract – Ultrasonic wave propagation across material surfaces reveals essential information about the materials' elastic behavior. The elastodynamic response of the surface is characterized by the Green's function that fully captures all its direction-dependent and frequency-dependent features. Here we present the first direct experimental visualization of the Green's function, including all its complex details resulting from elastic anisotropy. We achieve this visualization using a dedicated modification of transient grating spectroscopy (TGS), which is a method otherwise well established for measuring Rayleigh-type surface acoustic waves. To overcome the limitations of conventional TGS, we explore near-field thermoacoustic phenomena occurring within TGS experiments. We reveal that, along with the transient standing-wave patterns that diminish within hundreds of nanoseconds, there also emerge ultra-transient oscillations with lifetimes at least an order of magnitude shorter. These ultra-transient effects enable capturing the surface acoustic response with exceptional detail, and the resulting experimental angular dispersion maps strikingly replicate the theoretical Green's functions. By utilizing this feature, ultra-transient grating spectroscopy (UTGS) becomes a powerful new tool for detailed contactless characterization of anisotropic solids, opening new pathways for studying single-crystalline materials utilized in diverse modern application fields, including solid-state cooling via the elastocaloric effect, magnetoelastic devices, or nanoscale electromechanical systems.

Introduction

From the crystal lattice at the atomic scale to the mesoscopic layout of artificially built composites, the internal structure of materials manifests itself in their dynamic mechanical response. This includes direction-dependent (anisotropic) properties and frequency-dependent (dispersive) behavior.[1] Capturing the full complexity of the dynamic response therefore requires a description in the frequency–direction parameter space. For acoustic experiments on free surfaces, this means frequency-resolved description of the material for all directions lying along the surface.[2]

The theoretical object representing the response of the surface is the frequency-domain elastodynamic *Green's function*, which is a function describing the dynamic displacement field arising in a half-space when loaded by a force that is harmonic both in time and in space – a force with prescribed surface wave vector (k-vector) and frequency.[3] The Green's function is difficult to obtain experimentally, because that would require detecting the displacement field with a simultaneous application of the force. However, the state-of-the-art laser-ultrasonic techniques for materials characterization are not far from accomplishing this task. Spatially harmonic sources are routinely used in the transient grating spectroscopy method (TGS, setup shown in Figure 1(a)), which is a technique utilizing two coherent laser beams to create interference fringes on the surface of the sample (Figure 1(b)).[4–6] The interference pattern acts as an array of line-like

thermoacoustic sources (Figure 1(c)) with a harmonic energy profile in the direction perpendicular to the fringes; this direction determines the orientation of the surface k-vector of the acoustic waves generated by the pattern, and can be changed by rotating the sample with respect to the optical path.[7] In the time domain, the TGS source is a short pulse, spanning a broad frequency band from which any chosen frequency can be analyzed separately using spectral methods. This means that the TGS technique is, in theory, perfectly suitable for fulfilling the assumptions for the Green's function in terms of the prescribed force. But is it also capable of detecting the immediate response of the surface to this force?

In the traditional interpretation of the TGS experiment, the individual fringes generate both surface acoustic waves (SAWs) and bulk acoustic waves, where the former propagate along the surface and the latter into the whole half-space (Figure 1(d)).[8] The SAW amplitude does not significantly diminish with the propagation, and thus, counter-propagating SAWs from numerous sources superimpose in a standing-wave field, oscillating at frequency given by that of SAWs with wavelength determined by the spatial periodicity of the source. These vibrations are then optically detected by the diffraction of the probe beam, and the frequency spectrum of the recorded diffraction signal is typically understood as the main output of the TGS experiment.[7,9] The diffraction is possible thanks to the ripple (the 'transient grating') created on the surface; besides the oscillatory part arising from the acoustic standing waves, the ripple has also a non-acoustic part formed due to thermal expansion (the transient thermal grating, TTG), that can be utilized for measuring thermal diffusivity of the material.[10–12]

The standing waves are a typical far-field response to the loading, and can be understood as a local transient resonance of the free surfaces. For this reason, frequencies of Rayleigh-type SAWs are seen as dominant sharp peaks in the frequency spectra in TGS measurements; similar standing wave patterns, easily detectable by TGS, are also created by pseudo-Rayleigh waves (pSAWs).[13]

While these far-field phenomena will necessarily dominate the TGS signals, the fact that the signals are recorded immediately after the loading pulse is applied and directly at the location where the pulse is applied, indicates that they should also contain information about the near-field response. In the following, we describe a modification of the TGS experiment that enhances the near-field features, and thus leads to visualization of the Green's function with remarkable detail. This brings new direct insight into the complex elastodynamic behavior of free surfaces. To demonstrate the developed approach, we perform experiments on various cuts of single-crystalline samples, where the complexity of the response follows from elastic anisotropy, and for which the theoretical Green's function can be easily calculated, thus enabling a straightforward comparison between theory and experiment. The approach is also suitable for surfaces of heterostructures (such as layered media and composites) or acoustic metamaterials.[14–16]

Results and Discussion

Enhancing near-field features in TGS experiments

Consider, hence, that there exist phenomena generated by the conventional TGS thermoacoustic source, which appear and diminish at much shorter time-scales than the SAW and pSAW standing waves, because of their near-field character. To make the TGS more sensitive to these phenomena, we adopted the following three modifications.

1. **We utilized strongly elliptical beam shapes, detected the vibrations only in the central part, and used a coplanar geometry for pump and probe beams.** In conventional TGS measurements, both the excitation and detection spots are circular, often of similar sizes.[17,18] In such case, a lot of information is obtained from locations far from points of action of the maxima of the initial applied force, which makes such TGS measurement conceptually close to the spatially resolved acoustic

spectroscopy technique (SRAS), where the response is recorded in a point outside of the spatially periodic source.[19,20]

Here, we are interested in the response exactly in the points where the maximum force is applied, and want to lower the input from waves propagating over larger distances. However, we also need to maximize the number of fringes (wavelengths) with strong excitation. For this reason, we shape the laser beams to form strongly elliptical patterns, reaching the ratio of long-to-short axis of 8 to 1.[7] To maximize the diffraction potential, we shape the detection beam to a similar elliptical shape with the axes length just above half that of the excitation spot (Figure 1(e)).[21]

Also, many TGS systems utilize similar optical wavelengths (colors) of pump and probe lasers, which then requires to split the optical planes of these lasers for spatial separation.[10,22] To strengthen the diffraction efficiency, we use two distinct laser wavelengths (1064 nm for pump and 532 nm for probe), which allows us to leave them in the same sagittal plane, enhancing both sensitivity and k-vector selectivity of the measurement.[9]

2. **We utilized full bandwidth of highly sensitive photodiodes for the detection.** The TGS experiments are typically suited for characterization of thin surface films,[9,14,23] surface damage from irradiation,[24–26] or for spatial modulus mapping,[17,27] which motivates using as short wavelengths as possible, typically down to 3-6 μm. The response is then recorded by photodiodes and amplifiers with bandwidth up to 1 GHz, well-suited for capturing the dominant frequency peak corresponding to SAWs/pSAWs – but not that of the faster acoustic waves in typical single crystalline solids (metals, inorganic oxides). Here, instead, we use 10 μm wavelength, which allows us to register these acoustic modes even with the same bandwidth. Furthermore, we use in-house designed combination of Si PIN photodiodes with 60 dB amplifiers, thus combining high sensitivity, maximal power input, and amplification to significantly increase the signal-to-noise ratio. Also, the longer wavelength makes the pulsed laser source (with a typical pulse duration (FWHM) of ~ 0.5 ns) relatively shorter with respect to the characteristic times in the wave field, which leads to effectively more broadband generation of the waves (see Supplementary information for a numerical simulation-based analysis of this effect).

3. **We performed detailed angular scanning with extensive signal averaging.** Since the near-field features are expected to contribute to the output signal with much smaller amplitudes than the SAW/pSAW standing wave patterns, we set the experiments so that these features become better distinguishable from the noise. This comprises up to 50 thousand times averaging of the signal for each direction, but also changing the direction with a small angular step, since some features may become visually discernible only through their continuous evolution with the surface wave vector direction. (See the Supplementary information for the comparison with lower averaging and larger angular step.)

With these modifications, the TGS method has been applied to a nickel single crystal and an iron aluminide single crystal (Fe_3Al). For each free surface, we performed a 0–180° angular scan with a 1° step, with results shown in Figure 1(f). To avoid explicit dependence on the used wavelength, the maps are shown in the direction-vs-wavespeed coordinates, where the wavespeed v is recalculated from the frequency f and wavelength λ as $v = \lambda f$. These two materials were chosen as prototypes of cubic single crystals with moderately strong elastic anisotropy (Zener anisotropy ratio[28] for Ni is $Z = 2.6$) and strong elastic anisotropy ($Z = 4.3$ for Fe_3Al), respectively. Also, for both materials, the wavespeeds of acoustic waves (all modes of bulk acoustic waves in all directions, as well as SAWs/pSAWs on arbitrary

cuts) fall between 2 and 7 mm µs^{-1}, which corresponds to the frequency range of 200-700 MHz, covering perfectly most of the bandwidth available. On the Ni single crystals, the measurements were performed on high-symmetry cuts by (1 1 0) and (3 1 1) lattice planes, while on general irrational planes for Fe_3Al – the approximate Miller indices of the cuts are given in the headings to individual maps in Figure 1(f).

It is seen that although both materials have the same crystal symmetry, the obtained maps increase in complexity with increased strength of elastic anisotropy as well as with reduced symmetry of the cuts. All the maps shown, and particularly those for the general cuts of the strongly anisotropic Fe_3Al crystal, exhibit a variety of peaks, frequency bands, shoulders, and discontinuities, making it obvious that they include much richer information than just frequencies of standing SAW/pSAW wave patterns for given directions. But how are these features related to the respective Green's functions?

The thermoacoustic source in the TGS experiment for opaque materials is based on rapid local heating in a thin surface layer, leading to thermal expansion, and the diffraction of the probe beam is sensitive to out-of-plane displacements.[29] In the coordinate system introduced in Figure 1, the measured response to the TGS source should be described by the G_{13} component of the Green's function.[9] Utilizing the partial-wave approach (described in the Methods section),[3] the $|G_{13}|$ maps were calculated for all experimentally studied cuts, with the result shown in Figure 1(g). The agreement with the experimental maps is striking, regardless of which material and which cut is chosen. Even very minute variations in the calculated $|G_{13}|$ are matched in the FFT amplitude A, and the shapes and relative intensities of all features are identical, up to some experimental scatter in A.

The observed agreement confirms that, indeed, the modified TGS experiments are able to capture the additional features in the elastodynamic response, and to visualize one component of the Green's function in its whole complexity. This has two important implications: First, the Green's function calculation can be used to explain several details in the experimentally obtained maps (which is an approach we adopt in the discussion below). And second, the TGS maps obtained with the modified setup bring rich information about the elastic behavior of the material, and thus, can be utilized for the determination of its anisotropic elastic coefficients c_{ij}.

For homogeneous, linearly elastic materials, the latter task is typically accomplished by an "inverse procedure".[30,31] This means minimizing the mismatch between experimentally determined wavespeeds $v_n^{\mathrm{exp}}(\mathbf{m})$ in directions $\mathbf{m}$ and calculated values $v_n^{\mathrm{calc}}(\mathbf{m}, c_{ij})$ for iteratively improved guesses of elastic constants,

$$\sum_n \left(v_n^{\mathrm{exp}}(\mathbf{m}) - v_n^{\mathrm{calc}}(\mathbf{m}, c_{ij}) \right)^2 \underset{c_{ij}}{\longrightarrow} \min . \tag{1}$$

The richer the set of $v_n^{\mathrm{exp}}(\mathbf{m})$, the more complete information about the elastic constants is obtained.[7,31] Several fine features in the TGS (and the $|G_{13}|$) maps, copy exactly the directional evolutions of wavespeeds of various acoustic modes, both surface-guided and limiting bulk waves, as seen from comparison of these evolutions (Figure 1(h)) with the maps. This means that extensive sets of $v_n^{\mathrm{exp}}(\mathbf{m})$ can be extracted directly from measurements on a single free surface. If, moreover, the TGS experiments are performed on a principal cut, such as the (1 1 0) cut for the Ni single crystal in the first column of Figure 1(f–h), some points in the maps correspond to wavespeeds of bulk longitudinal and shear modes in principal directions that are related to c_{ij} through simple algebraic equations, and thus, the full set of elastic coefficients can be calculated without the inverse procedure. For general cuts and strongly anisotropic materials, in contrast, it might be difficult to identify the modes directly from the map, such as for the selected cuts in Fe_3Al. Instead, approaches allowing for full visual comparison of these maps with their experimentally obtained counterparts would be more suitable, possibly replacing the summation in Equation (1) with integrals, and

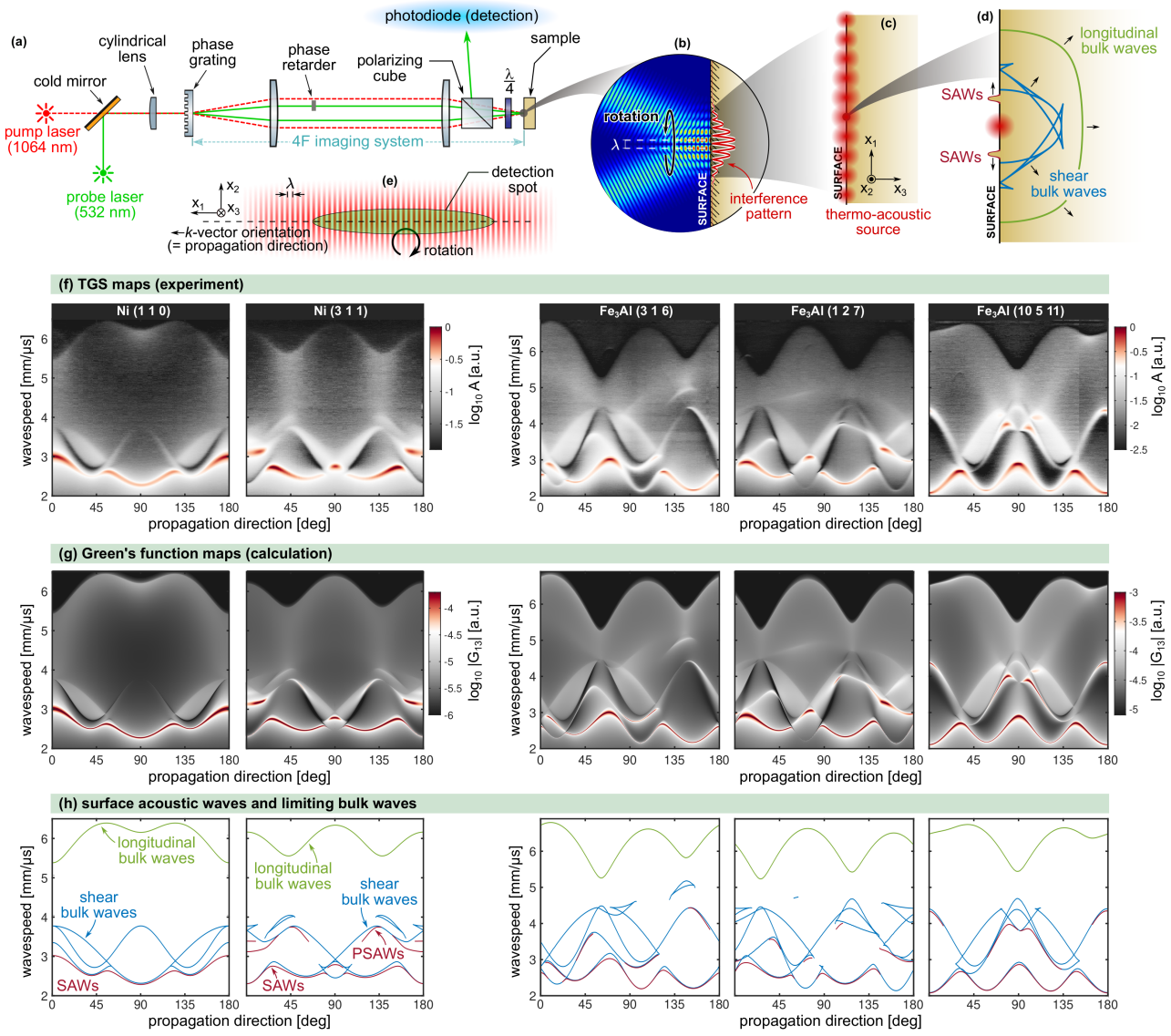

Figure 1. TGS experiments on cuts of anisotropic single crystals.
(a) the optical path used for TGS measurements, see Supplementary information Fig.S1 for a physical realization; **(b,c)** formation of a spatially harmonic thermoacoustic source in the TGS experiment, the source arises from an interferometric pump-laser pattern with spatial period λ, and the rotation of the sample enables measurements in different directions along the surface; **(d)** a hypothetical response of the anisotropic free surface to one line-like source from the TGS source pattern; **(e)** the geometry of the pump laser interference pattern, and the shape and relative size of the detection spot. **(f)** experimental maps for high-symmetry planes of Ni (the left two columns) and low-symmetry planes of Fe_3Al (the right two columns); **(g)** corresponding maps of the $|G_{13}|$ Green's function component; **(h)** corresponding wavespeeds of surface-guided and bulk acoustic waves. The bulk waves are the so-called limiting bulk waves, which means bulk waves that carry energy flux in direction parallel to the free surface (several such waves can exist for the shear modes for each direction of propagation).

utilizing image-processing tools to measure the misfit between the calculation and the experiment. It is also worth noting that a single component of the Green's function appears to be fully sufficient for representing the anisotropic behavior of the studied material, as the wavespeeds of the SAWs/pSAWs as well as of most of the limiting bulk waves of various polarizations correspond to a visible contrast in the $|G_{13}|$ map. This

means that the set $v_n^{\mathrm{exp}}(\mathbf{m})$ cannot be further extended if maps of other components were available, such as for example $|G_{33}|$ that is, in principle, accessible through surface Brillouin spectroscopy.[32,33]

The completeness of the information on elastic constants in the experimentally obtained maps turns TGS into a powerful tool in materials characterization. For single crystals, particularly those engineered for specific functionalities, the elastic anisotropy is often intrinsically linked to their caloric, magnetic, or electric properties. Such linking can be found in ferroelastic alloys with a strong elastocaloric effect for solid-state refrigeration[34–38] and energy harvesting,[39,40] or magnetoelastic materials for new sensors and actuators.[41,42] For all these materials, the enhanced TGS characterization can bring novel insights in their functional properties and foster their further development. This approach enables rich information to be obtained on a single cut of the crystal with arbitrary orientation. Moreover, the measurement spot is relatively local in terms of both its in-plane dimensions ($\sim 800 \times 800\ \mu\mathrm{m}^2$, can be reduced below $\sim 500 \times 500\ \mu\mathrm{m}^2$ without any significant loss of information) and its penetration depth (up to several wavelengths), which can be utilized for example for measurements on individual grains over surfaces of coarse-grained polycrystals, functionally graded materials with gradient composition, or individual components of macroscopic composites. In fact, the three cuts of Fe_3Al presented here are a part of a single large polycrystalline piece of this material.

Identifying the Ultra-transient Features in the TGS Signal

To justify the above developed approach, we need to prove that the additional features in TGS maps indeed originate from the immediate near-field response of the material to the thermoacoustic source. The visual agreement between the TGS maps and $|G_{13}|$ may suggest this is true, but direct evidence for that must be found by analyzing the time-domain signals. Such analysis is performed for one selected experiment (the approximately (3 1 6) cut of the Fe_3Al crystal) in Figure 2. The subfigures (a)-(d) show how the spectrum of the angle-resolved signals (the TGS map) evolves as the earliest parts of the signals are progressively truncated. A representative time-domain signal corresponding to the first measured propagation direction is plotted above the maps. It is seen that the visible high-frequency oscillations last for hundreds of nanoseconds, corresponding to the lifetime of the transient grating arising due to the SAW/pSAW standing wave patterns. Weak low-frequency oscillations appear in the signal, resulting from Scholte waves generated in the air above the free surface.[43] These will be excluded from further analysis.

In Figure 2(a), the full signal results in the full TGS map. Based on the curves in Figure 1(h), we can identify peaks or shoulders corresponding to specific wave propagating modes in this map (L – longitudinal waves, T – transverse (shear) waves, SAW – surface acoustic waves) and select three points in which we will observe their evolution with truncation of the time-domain signal, each for one mode. Let us notice that, due to elastic anisotropy, the bulk modes are not purely longitudinal or purely shear waves, so the designations L and T refer to their dominant polarization orientation only.[1] Figure 2(b) then shows how the map changes with cutting off just 5 ns from the beginning of the signal. The shoulders/edges marking the velocities of the longitudinal and shear modes become much less distinct, and even completely disappear for some directions of propagation. In the selected point L and T, some features are still visible, but their character changes from shoulders to very weak peaks that can be traced only because of the fine angular resolution in the experiment.

When 15 ns are cut from the beginning of the signal, any features indicating the longitudinal and shear modes in the selected point completely disappear (Figure 2(c)) and they disappear also for most of the propagation directions with cutting off the first 25 ns, Figure 2(d). In other words, the information about all features in the map seen in Figure 2(a) but not in Figure 2(d) is contained in just less than 25 ns of the signal. And, as the most significant change is between subfigures (a) and (c), one can deduce that most of this information is included in the first 15 ns or less.

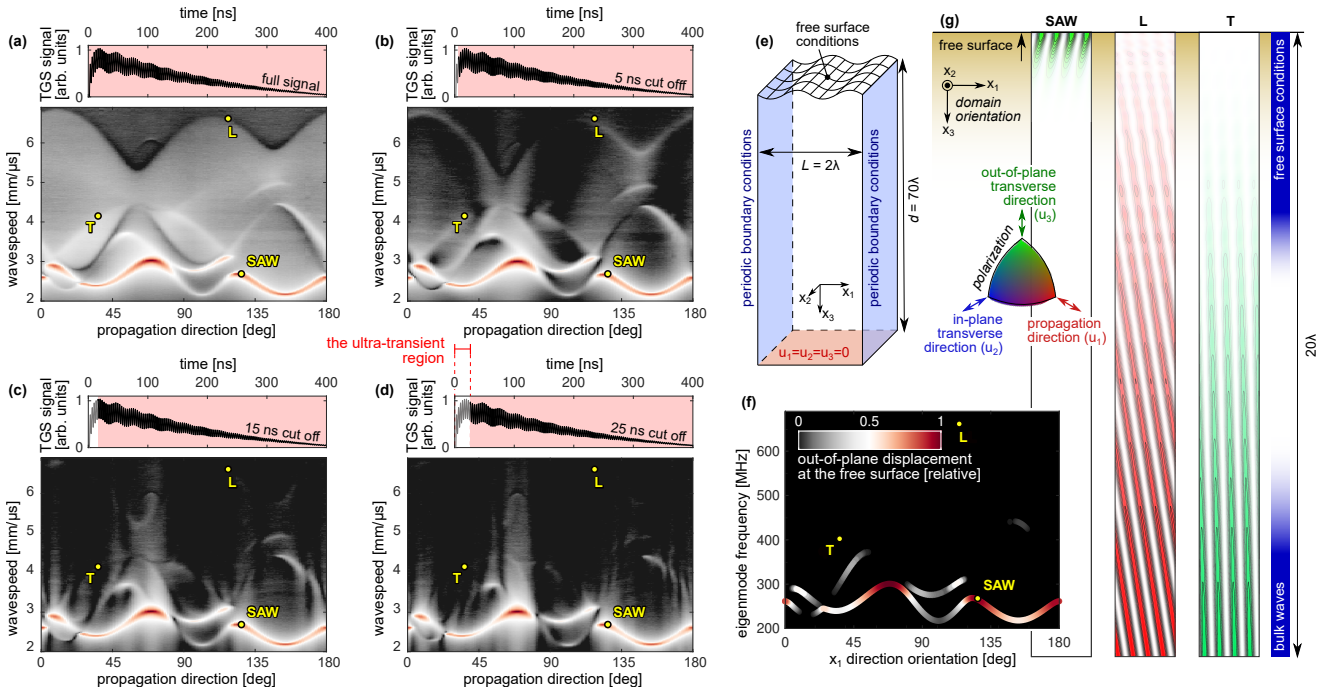

Figure 2. The ultra-transient origin of detailed features in TGS maps.
(a-d) Effect of time-domain signal truncation on the experimental TGS map for the Fe_3Al (3 1 6) surface: Full TGS map (no truncation, (a)), followed by maps after omitting the first 5, 15, and 25 ns. After the ultra-transient region is cut off (d), the map reduces to peaks indicating the (far-field) resonant response of the surface. **(e-f)** Calculation of the resonant response of the surface using the Ritz-Rayleigh method: (e) the computational domain with boundary conditions; (f) the spectrum of eigenmodes of the domain, color-coded based on the out-of-plane component of the displacement field on the surface – the spectrum perfectly matches the TGS map in (d); (g) modal shapes of the eigenmodes corresponding to the three selected points. The color in the maps indicates the polarization direction of the displacement, the intensity of the color represents an absolute value of the amplitude, ignoring the sign (two maxima per one wavelength λ).

This means that the details in the TGS map arise from phenomena that are transient with respect to the lifetime of the transient grating. To distinguish between these two time-scales (several nanoseconds for the near-field behaviors, several hundreds of nanoseconds for the typical SAW/pSAW standing wave patterns), we introduce here the term *ultra-transient* for the shorter one. Because of the spatially harmonic energy profile of the source, the near-field response is initiated periodically along the surface of the material, and can be therefore detected from diffraction of the probe laser beam. This means that the ultra-transient displacement field arises as a dynamic periodic grating that we will hereafter call the *ultra-transient grating*, and we will refer to the analysis of the frequency spectrum of this grating as *ultra-transient grating spectroscopy* (UTGS).

After the ultra-transient region is removed from the time-domain signal, Figure 2(d), the TGS map becomes relatively simple. It does not contain any shoulders, edges, or bands, just peaks that change their positions with the propagation direction; some of these peaks exist only in certain angular intervals, and there are discontinuous jumps in the positions of the peaks. The peaks are expected to represent local transient resonances of the surface, that is, standing waves. To confirm this assumption, we have performed an additional numerical calculation, summarized in Figures 2(e,f,g). We calculated vibrational eigenmodes of a domain shown in Figure 2(e) representing an elastic half-space with prescribed periodicity of the displacement field along the x_1 direction. The calculation was done using the Ritz-Rayleigh approach

(see Methods) and resulted in a spectrum shown in Figure 2(f). In this plot, the lines show the evolution of the eigenmode frequencies as the domain orientation is rotated, and the color code represents the relative out-of-plane component of the surface displacement field for each eigenmode. We can see that the calculation result agrees very well with the map in Figure 2(d). This means that the vibrational response of the material beyond the ultra-transient region is indeed given by resonances of the surface in the form of standing wave patterns. From the three selected points in the map, the conditions for the far-field vibrations with non-zero out-of-plane amplitude are satisfied only for the SAWs. This is in a good agreement with the fact that, without UTGS modifications, the TGS experiments can reliably capture the surface-guided modes, but not the limiting bulk acoustic waves.

On the other hand, however, the points L and T also correspond to some eigenmodes of the domain. These are standing longitudinal and shear waves inside the bulk – the displacement fields of these modes as they result from the Ritz-Rayleigh calculation are shown in Figure 2(g). The corresponding limiting bulk longitudinal and shear waves, albeit being solutions to the Christoffel equation (2), do not satisfy the free-surface conditions; that is why their amplitude in the eigenmode diminishes to zero when approaching the surface, and these modes thus do not result in any diffraction of the probe beam. This holds true for all similar modes related to bulk acoustic waves with non-zero out-of-plane components of the polarization. In contrast, the eigenmodes representing standing Rayleigh-type and pseudo-Rayleigh surface waves (SAWs/pSAWs) are compliant with the free-surface conditions and have non-zero out-of-plane displacement field components. That is why they are observed in the far-field response to the source that persists in the measurement spot for several hundreds of nanoseconds.

For completeness, let us mention that the requirement of non-zero out-of-plane component of the displacement field applies also for the near-field response detected by UTGS. If any of the ultra-transient features has a strictly in-plane polarization, it remains invisible for the measurement. This is clearly seen for the high-symmetry (1 1 0) cut for the Ni single crystal in first column of Figure 1(f–h), where the UTGS peak marking the fastest bulk shear wave completely disappears for propagation angles close to 90°, where this mode becomes purely shear-horizontal. The absence of this mode in the out-of-plane response is identically reflected in the calculated $|G_{13}|$.

Discussion of the Observed Acoustic Behavior of Anisotropic Free Surfaces

Regarding the level of detail and completeness of the maps, the UTGS results shown here clearly surpass the crystal-acoustics visualizations achieved through the imaging of ballistic phonons,[44] picosecond ultrasonics,[45,46] or transmission acoustic microscopy.[47] These approaches, moreover, typically require extreme conditions such as very short wavelengths and deep cryogenic temperatures to mitigate thermal scattering and phonon interactions, and utilize point-like sources for the excitation, which necessarily leads to loss of information on the wave-vector orientation of the detected waves. In principle, UTGS overcomes this by the strictly harmonic excitation pattern generating coherent waves with well-defined wave-vector orientations.

In addition, the direct correspondence of the UTGS result to the $|G_{13}|$ component of the Green's function enables explaining theoretically the morphology of the experimentally observed UTGS maps. The so-called Lamb problem,[48] which means calculating the elastodynamic response of an anisotropic, linearly elastic half-space to a prescribed loading, can be solved semi-analytically using the concept of partial waves,[3] elaborated in more detail in the Methods section. In this approach, the displacement field on the free surface for given surface wave vector and frequency can always be decomposed into displacement fields of three independent solutions of Christoffel's elastodynamic equation (2).[49] Each of these solutions is always either a planar harmonic bulk wave (the so-called *homogeneous solution*), or a surface-guided harmonic wave with its amplitude exponentially decreasing with the distance from the

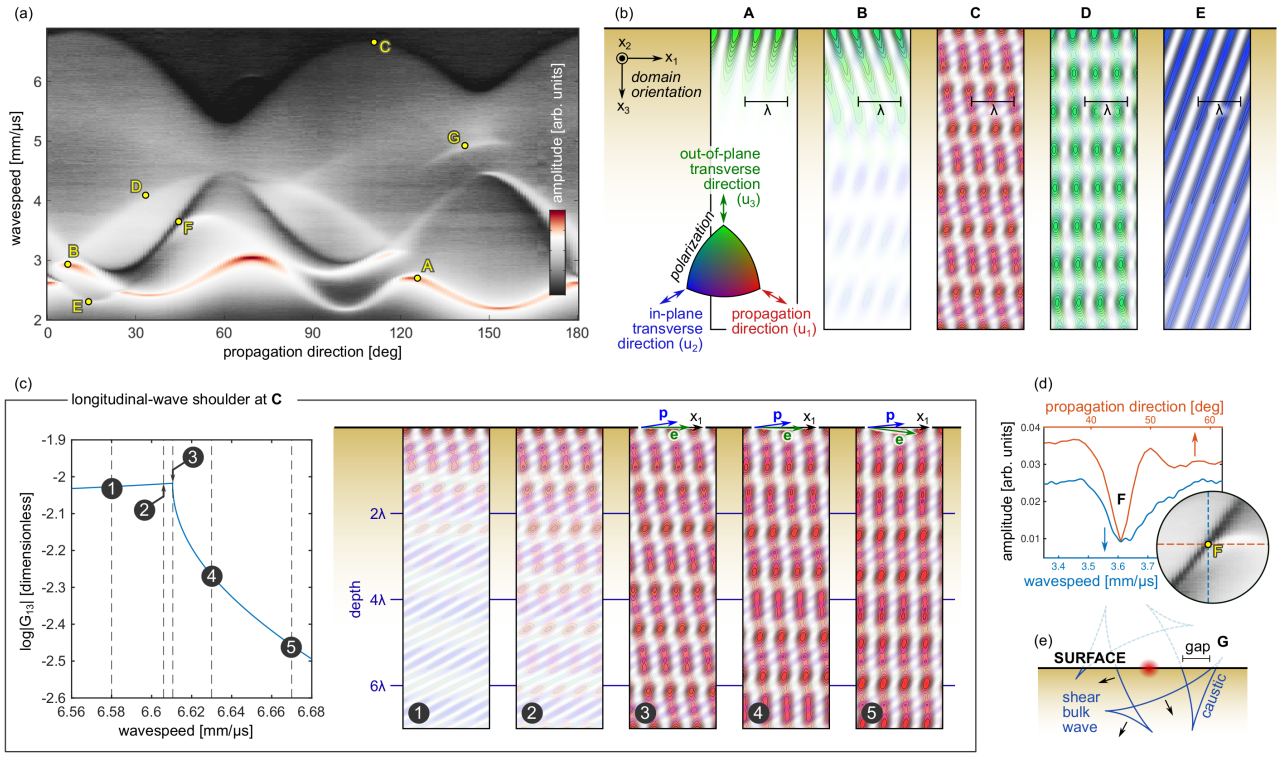

Figure 3. Detailed features in the UTGS map explained by analysis of the Green's function. **(a)** UTGS map for the Fe_3Al (3 1 6) surface with selected features labeled by capital letters (A–G, points A, C, and D correspond to modes labeled SAW, L, and T in Figure 2, respectively); **(b)** displacement fields for points A–E calculated as superpositions of three partial waves from the construction of the Green's function; **(c)** the change in the displacement field (the evanescent-to-homogeneous conversion of one partial wave) responsible for the formation of a sharp shoulder (a 'cliff') at point C; for stages (3)–(5), the arrows show the orientation of the energy flux direction $\mathbf{e}$ and a normal to the longitudinal phase fronts $\mathbf{p}$ with respect to the propagation direction x_1. **(d-e)** narrow-band features observed in the map: the acoustic sink (in (d), cuts w.r.t. both coordinates are shown) and the caustics (in (e), schematic explanation of the creation of a disconnected segment).

surface (the so-called *evanescent solution*). Except for the SAW/pSAW peaks, most of the sharp contrasts seen in the Green's function plot, and, correspondingly, in the UTGS maps, can be interpreted as changes in the types of the partial waves when, for example, one of the partial waves converts from homogeneous into evanescent.

The partial waves also enable constructing the displacement fields corresponding to individual points in the Green's function plot, so that one can directly calculate which orientations and types of elastic strain field are carried by the individual features in the UTGS map. An example of such analysis is given in Figure 3, using, similarly as for Figure 2, the (3 1 6) cut for the Fe_3Al crystal. In Figure 3(a), the UTGS map for this cut is shown, with selected points of interest (capital letters A-G) in which we utilize the calculated counterpart of the TGS map to interpret the observation.

The points A–E correspond to sharp edges and peaks in the map. According to Figure 1(h), these sharp features mark the velocities of SAWs, pSAWs and limiting bulk acoustic waves, respectively. The partial wave approach enables us to confirm this by explicitly calculating the displacement fields, as shown in Figure 3(b). The point A is selected identically to the point labeled 'SAW' in Figure 2. It corresponds to a Rayleigh-type SAW, which is composed of three evanescent solutions of the Christoffel equation (2). As this wave is included both in the near-field and far-field responses, the displacement field for this

wave calculated from the partial waves is identical to that obtained from the Ritz-Rayleigh calculation of the eigenmodes. A similar situation appears for the point B, which corresponds to a pSAW mode. The displacement field has two evanescent components with dominantly in-plane polarizations, but includes also one homogeneous, out-of-plane polarized wave responsible for the sharp peak in the TGS map. Again, a resonant mode approximating closely the pSAW standing pattern is included in the eigenproblem solution and has a strong out-of-plane component, and thus the peak at point B persists in the spectrum even after the ultra-transient region is cut off (Figure 2(d)).

The point C corresponds to the point labeled 'L' in Figure 2, as it marks a bulk longitudinal mode, absent in the far-field response. The displacement field for this point in Figure 3(b) reveals that this mode is, indeed, dominantly polarized in the longitudinal direction (along the propagation direction). However, to comply with the prescribed harmonic loading at the surface, the dominant homogeneous longitudinal wave is coupled with two other homogeneous partial waves that disturb the planar wavefronts of the longitudinal mode and result in a more complex displacement field. The wavespeed associated with this displacement field corresponds to the dominant longitudinal wave, and the other two partial waves can be understood as resulting from the interaction of this dominant wave with the surface. The UTGS and $|G_{13}|$ maps in this point exhibit a 'cliff' (a sharp shoulder for the given direction of propagation), which results from conversion of one of the partial waves as we discuss below in Figure 3(c). A very similar situation occurs for point D (identical to the point labeled 'T' in Figure 2), which corresponds to the velocity of a limiting bulk shear wave with out-of-plane polarization. Again, the displacement field is a superposition of three partial waves, among which the out-of-plane polarized one is the strongest, and the 'cliff' associated with this point arises by a similar mechanism as for point C.

A weak but still visible contrast is seen at point E. The velocity corresponding to this point equals the velocity of an in-plane polarized bulk shear wave that, in principle, should not be detectable by the probe beam diffraction. Accordingly, this point does not correspond to any detectable eigenmode in Figure 2(f). However, the near-field response analysis reveals that the contrast arises due to a transition of a weak out-of-plane polarized homogeneous wave from evanescent to homogeneous; at the surface this wave effectively couples with other two partial evanescent waves, resulting in a dominantly in-plane shear polarization, as seen in Figure 3(b).

Figure 3(c) gives an explanation of how the sharp 'cliffs' marking the limiting bulk wave velocities are created. It shows the evolution of the displacement field in the vicinity of the point C as the wavespeed coordinate increases. For wavespeeds lower than the velocity of longitudinal limiting bulk waves (stages ① and ② in Figure 3(c)) at least one of the partial waves is evanescent, and the energy of the waves remains dominantly bound to the surface. As the wavespeed coordinate increases, the evanescent character of the displacement field becomes weaker, and, finally, the given partial wave becomes homogeneous at the wavespeed equal to the velocity of the limiting longitudinal bulk wave (stage ③). At this point, the energy flux carried by the wave points exactly along the surface, as required by the definition of the limiting bulk wave. With further increasing the wavespeed coordinate, however, the orientation of the longitudinal wave fronts starts rotating (stages ④ and ⑤), and so does the orientation of the energy flux, which means that the acoustic energy becomes more and more steered away from the surface. In other words, the 'cliff' represents a conversion from an evanescent solution, in which the energy is bound to the surface, to a homogeneous solution that drives the energy below the surface. In the experimental map, the 'cliff' from the near-field response can be partially smoothed or overlapped due to a peak formed by the surface skimming longitudinal waves. These are waves generated on a surface by a longitudinal wave running underneath and along the surface. Because of their dispersive character, the surface skimming longitudinal waves do not create resonance-like standing wave patterns, but, thanks to the spatial periodicity of the longitudinal waves that generate them, they can contribute to the diffraction

of the probe beam. In Figure 2(b), it is seen that after cutting off the first 5 ns of the time-domain signal, the edges indicating the longitudinal modes turn merely into peaks. Plausibly, this can be ascribed to a pattern of counter-propagating skimming waves which, in terms of its lifetime, falls between the transient and ultra-transient regimes. Small peaks corresponding to wavespeeds slightly lower than the velocity of the longitudinal limiting bulk wave typically mark the surface skimming longitudinal waves in TGS experiments.[7]

When two 'cliffs' form close to each other, they can encapsulate a narrow band as the one seen in the point F. In Figure 3(d) cross-sections of the experimental TGS maps in the surrounding of the point F are shown, documenting the sharp drop in the amplitude along both the wavespeed and the angle coordinates. The free surface in this area acts as a highly selective filter that transmits all waves except those with specific velocity. On the other hand, the band between two 'cliffs' cannot be understood as a band gap similar to those appearing in periodic media, where the energy at given frequency is trapped in a local resonance of the structure. Here, instead, the energy at a specific frequency is steered from the surface, as, in a narrow frequency interval, the character of one partial wave changes from evanescent to homogeneous and back. Hence, the feature in point F can be seen as an 'acoustic sink', where only waves at a specific wavespeed are allowed to penetrate into the material.

An inverse feature to the 'acoustic sinks' can be seen in point G, where the amplitude of the UTGS map locally increases and creates an object disconnected from other edges or peaks in the map. Similar features appear in all low-symmetry cuts, and are associated with disconnected segments of bulk shear waves. These arise from the complex, cuspidal shapes of bulk shear wave slowness surfaces (caustics) intersecting the free surface (Figure 3(e)). Such intersections can enable bulk wave energy to briefly travel along the surface or provide pathways for surface energy to couple into focused bulk beams. The edges of these caustics are typically directions of strong energy focusing,[44,49] likely contributing to the relative prominence of these features in the maps. In terms of partial waves, these objects are formed by a mechanism very similar to the 'acoustic sinks', but in this case the evanescent solution locally changes into a homogeneous solution that carries energy along the surface, rather than steering it into the material.

Concluding Remarks

In summary, we have demonstrated that ultra-transient grating spectroscopy (UTGS) provides an unprecedented experimental capability to visualize the complete surface acoustic response in elastically anisotropic crystals. By capturing and analyzing the rich information encoded within the initial nanoseconds of the elastodynamic response (the so-called ultra-transient region), UTGS generates experimental maps that strikingly replicate the corresponding component of the theoretical elastodynamic Green's function in all its complexity. This goes far beyond conventional surface acoustic wave (SAW) characterization that TGS is suited for, bringing direct and detailed insight into the acoustics of the studied crystals.

The ability to obtain such comprehensive experimental Green's function maps (without requirements on cryogenic temperatures and with high selectivity in wave-vector orientation) opens significant new possibilities for materials characterization and for a deeper understanding of coupled phenomena in advanced materials; this we have recently demonstrated on examples of superelastic[50] and magnetic shape memory[51] single crystals, as well as thin epitaxially grown films.[16] The all-optical contactless nature of the UTGS analysis predetermines the newly developed approach to be used under various extreme conditions (low and high temperatures, strong magnetic fields, irradiation), enabling direct in-situ observation of the Green's functions of materials under these conditions with time or with additional external stimuli. This opens a novel, previously explored pathway for studying the relationship between elastic behavior and functional performance in newly developed materials.

Methods

Transient grating spectroscopy

The measurements were performed using the optical path outlined in Figure 1(a), which is a classical arrangement for TGS.[5,7] The pump pattern was created by interference of strongly elliptical laser beams (approximately $0.8 \times 0.1\,\mathrm{mm}^2$ in cross-section) in the near infrared range (1064 nm, pulse energy 110 µJ, pulse duration (FWHM) 0.53 ns, repetition rate 1 kHz). The nominal acoustic wavelength in the reported measurements was 10 µm, with the exact wavelength calibrated using a known material – for the reported measurement, the calibrated value was $10.064 \pm 0.005\,\mu\mathrm{m}$. The pulse energy was lowered in the optical path and tuned to be slightly below the ablation limit of the sample (typically below 40 µJ on the sample surface), so that no visible trace was left after the measurement.

The probe-beam pattern, created by a continuous-wave green laser (532 nm, nominal power 100 mW, reduced to 30 mW at the sample surface), was aligned with the same optical axis to further enhance the k-vector selectivity of the method.[9] To increase the overall sensitivity, the system utilizes the heterodyne detection approach.[5,10,29,52] The heterodyne phase was adjusted for optimal sensitivity to the out-of-plane displacements using a phase retarder. The diffracted probe beam was collected by a Si PIN photodiode (with maximal continuous input power of 50 mW and photosensitivity of $0.38\,\mathrm{A\,W}^{-1}$ for the probe-laser wavelength), and the signal was amplified with the gain of 60 dB in the frequency bandwidth of 10 kHz to 1 GHz.

To perform the angular-dispersion measurements, the sample was rotated with respect to the optical axis. At each measured angle, fifty thousand time-domain signals were averaged. The effect of the very fine angular scanning and of taking such a large amount of averages compared to hundreds of averages is shown in the Supplementary information. To characterize and remove parasitic signals, background signal was measured regularly. See more details on the processing of the time-domain signal in the Supplementary material.

Calculation of the Green's function

The surface dynamics calculation was based on the approach by Every et al.,[3,53] which can be summarized as follows:

For the given tensor of elastic constants C_{ijkl}, material density ρ, angular frequency ω, and surface wavevector $\mathbf{k}_{\parallel} = (k_1, k_2)$, the Christoffel equation

$$\left(C_{ijkl} k_j k_l - \rho\,\omega^2 \delta_{ik}\right) U_k = 0 \tag{2}$$

gives six solutions for the out-of-plane component of the wave vector $k_3^{(n)}$, $n = 1, \ldots, 6$, with corresponding eigenvectors $\mathbf{U}^{(\mathbf{n})}$. The waves with the resulting three-dimensional wave vectors $\mathbf{k}^{(\mathbf{n})}$ and polarizations $\mathbf{U}^{(\mathbf{n})}$ are the partial waves. Three of these waves represent either the evanescent waves (complex solutions for which the displacement field decreases exponentially along the x_3 direction) or the 'outgoing' waves (real solutions, for which the group velocity is directed into the solid).

The displacement resulting from a spatially and temporally harmonic surface force (defining $\mathbf{k}_{\parallel}$ and ω) acting in the x_j-direction is then formed as a superposition of these three phase-matched partial waves,

$$u_i^{(j)}(\mathbf{k}_{\parallel}, \omega; x_3) = \sum_{n=1}^{3} A_j^{(n)} U_i^{(n)} \exp(\mathrm{i} k_3^{(n)} x_3), \quad (i, j = 1, 2, 3). \tag{3}$$

The partial-wave amplitudes $A_j^{(n)}$ stem from the stress-strain relationship and the free-surface boundary

condition as

$$A_j^{(n)} = \frac{\mathrm{i}}{\omega}\left(\mathbf{B}^{-1}\right)_j^{(n)}, \quad (j,n=1,2,3). \tag{4}$$

where the boundary condition matrix can be written as

$$B_l^{(n)} = C_{3jkl}U_k^{(n)}\frac{k_l^{(n)}}{\omega}, \quad (l,n=1,2,3). \tag{5}$$

The surface Green's function components are then obtained as the displacement amplitude at $x_3 = 0$, which reads,

$$G_{ij}(\mathbf{k}_\parallel,\omega) = \sum_{n=1}^{3} A_i^{(n)}U_j^{(n)}. \tag{6}$$

This resulting value of the Green's function components depends on the chosen signs of the polarization directions $\mathbf{U^{(n)}}$ and the wave vector $\mathbf{k}_\parallel$. To avoid this ambiguity, we calculate the effective magnitude of the considered component $(i=1, j=3)$ for each in-plane direction as

$$|G_{13}(\mathbf{k}_\parallel,\omega)| = \frac{1}{2}\left|G_{13}(\mathbf{k}_\parallel,\omega) + G_{13}(-\mathbf{k}_\parallel,\omega)\right|, \tag{7}$$

which is the quantity plotted in Figure 1(g) and compared to the UTGS results in the main text.

Ritz–Rayleigh calculation method

The eigenmodes of the domain representing the free surface (Figure 2(e)) were calculated using the Ritz–Rayleigh method for SAWs in an elastically anisotropic half-space, introduced and described in detail in Ref. 31. The domain depth was set as $d = 70\lambda$ because the penetration depth of some of the evanescent modes increases with increasing strength of elastic anisotropy ($d = 20\lambda$ would be fully sufficient for the Ni crystal).[54] This depth enabled solutions representing both the near-surface behavior and the bulk behavior. Because of its assumed homogeneity in x_2, the displacement field u_i $(i=1,\ldots,3)$ was discretized into a functional basis as

$$u_i(x_1,x_3) = \sum_{k=0}^{N-1} \alpha_{k,i}P_k(2\hat{x}_3-1)\exp(2\pi\mathrm{i}\hat{x}_1), \tag{8}$$

with $\hat{x}_3 = x_3/d \in [0,1]$ and $\hat{x}_1 = x_1/\lambda \in [0,1]$. Here, $P_k(x)$ denotes a normalized Legendre polynomial of the k-th order, and $\alpha_{k,i}$ are coefficients of the functional basis. Legendre polynomials were used up to $N = 180$ in the discretization. The chosen functional basis inherently satisfied the periodic boundary condition. The bottom-plane constraint was imposed using a null-space method.[31,55]

The eigenmodes and eigenfrequencies of the domain were then sought using the Hamilton principle for the discretized displacement field, which has a form of the eigenvalue problem in a matrix form

$$0 = (\omega^2\mathbf{M} - \mathbf{K})\boldsymbol{\alpha}, \tag{9}$$

where $\boldsymbol{\alpha}$ is the vector of the coefficients from the discretization. Dimensions of matrices $\mathbf{M}$ and $\mathbf{K}$ are given by the size of the computational basis as $(3N-1)^2$. More details and explicit form of these matrices can be found in previous works of the authors.[16,30,31,56] The resulting eigenvalues represent the square of the frequency ω of the corresponding mode. To describe the character of the modes, the displacement field can be reconstructed using its eigenvector $\boldsymbol{\alpha}_k$ (as used for Fig. 2((g))). However, for various characterizations of the properties of the mode, eigenvectors can be used without the need to reconstruct the modal shape – e.g. to trace the angular-dispersion curves for individual modes, the similarity of modal shapes can be evaluated quantitatively by the absolute value of the dot product of their eigenvectors.[57]

Samples

The single-crystalline samples of nickel were acquired from MaTecK (Material, Technologie & Kristalle GmbH), with the accuracy of the crystallographic orientation of $< 0.1°$. The considered density was $\rho = 8.9\,\mathrm{g\,cm^{-3}}$, and elasticity of nickel was taken as $c_{11} = 251.9\,\mathrm{GPa}$, $c_{12} = 157.7\,\mathrm{GPa}$, and $c_{44} = 124.3\,\mathrm{GPa}$.[7]

The Fe_3Al samples were cut from an intermetallic alloy (exact composition Fe–28 at.%Al–4 at.% Cr) manufactured by Bridgman growth at the Institute of Physics, Czech Academy of Sciences. The density was $\rho = 6.62\,\mathrm{g\,cm^{-3}}$, and elasticity of $c_{11} = 179.5\,\mathrm{GPa}$, $c_{12} = 119.6\,\mathrm{GPa}$, and $c_{44} = 129.9\,\mathrm{GPa}$.[54] The precise orientations of the surfaces were determined by X-ray diffraction (Laue method), as summarized in Supplementary information Tab.S1. All measured surfaces were mechanically and chemically polished to obtain a good reflectivity (mirror-like finish) for the probe laser.

References

1. Every, A. *et al.* Bulk and surface acoustic wave phenomena in crystals: Observation and interpretation. *Wave Motion* **50**, 1197–1217, DOI: 10.1016/j.wavemoti.2013.02.007 (2013).
2. Every, A. Measurement of the near-surface elastic properties of solids and thin supported films. *Meas. Sci. Tech.* **13**, R21, DOI: 10.1088/0957-0233/13/5/201 (2002).
3. Every, A. G., Kim, K. Y. & Maznev, A. A. The elastodynamic response of a semiinfinite anisotropic solid to sudden surface loading. *J. Acoust. Soc. Am.* **102**, 1346–1354, DOI: 10.1121/1.420053 (1997).
4. Rogers, J. A. *et al.* Optical system for rapid materials characterization with the transient grating technique: Application to nondestructive evaluation of thin films used in microelectronics. *Appl. Phys. Lett.* **71**, 225–227, DOI: 10.1063/1.119506 (1997).
5. Maznev, A., Nelson, K. & Rogers, J. Optical heterodyne detection of laser-induced gratings. *Opt. Lett.* **23**, 1319–1321, DOI: 10.1364/OL.23.001319 (1998).
6. Hofmann, F., Short, M. P. & Dennett, C. A. Transient grating spectroscopy: An ultrarapid, non-destructive materials evaluation technique. *MRS Bull.* **44**, 392–402, DOI: 10.1557/mrs.2019.104 (2019).
7. Stoklasová, P. *et al.* Laser-ultrasonic characterization of strongly anisotropic materials by transient grating spectroscopy. *Exp. Mech.* DOI: 10.1007/s11340-021-00698-6 (2021).
8. Royer, D. & Dieulesaint, E. *Elastic Waves in Solids II: Generation, Acousto-optic Interaction, Applications* (Springer Science & Business Media, 2001).
9. Maznev, A. A., Akthakul, A. & Nelson, K. A. Surface acoustic modes in thin films on anisotropic substrates. *J. Appl. Phys.* **86**, 2818–2824, DOI: 10.1063/1.371130 (1999).
10. Johnson, J. A. *et al.* Phase-controlled, heterodyne laser-induced transient grating measurements of thermal transport properties in opaque material. *J. Appl. Phys.* **111**, DOI: 10.1063/1.3675467 (2012).
11. Huberman, S. *et al.* Unifying first-principles theoretical predictions and experimental measurements of size effects in thermal transport in SiGe alloys. *Phys. Rev. Mater.* **1**, 054601, DOI: 10.1103/PhysRevMaterials.1.054601 (2017).
12. Dennett, C. A. & Short, M. P. Thermal diffusivity determination using heterodyne phase insensitive transient grating spectroscopy. *J. Appl. Phys.* **123**, DOI: 10.1063/1.5026429 (2018).
13. Farnell, G. Properties of Elastic Surface Waves. In *Physical Acoustics*, vol. 6, 109–166, DOI: 10.1016/B978-0-12-395666-8.50017-8 (Elsevier, 1970).

14. Rogers, J. A., Maznev, A. A., Banet, M. J. & Nelson, K. A. Optical Generation and Characterization of Acoustic Waves in Thin Films: Fundamentals and Applications. *Annu. Rev. Mater. Sci.* **30**, 117–157, DOI: 10.1146/annurev.matsci.30.1.117 (2000).

15. Vega-Flick, A. *et al.* Vibrational dynamics of a two-dimensional microgranular crystal. *Phys. Rev. B* **96**, 024303, DOI: 10.1103/PhysRevB.96.024303 (2017).

16. Grabec, T. *et al.* Guided acoustic waves in thin epitaxial films: Experiment and inverse problem solution for niti. *Ultrasonics* **138**, DOI: 10.1016/j.ultras.2023.107211 (2024).

17. Weaver, C., Stapelberg, M., Short, M. P., Wylie, A. & Artalejo, E. B. Automated transient grating spectroscopy mapping and signal control for large samples. *Rev. Sci. Instruments* **95**, 074902, DOI: 10.1063/5.0202262 (2024).

18. Simmonds, M. J., Založnik, A., Patino, M. I., Baldwin, M. J. & Boechler, N. An increased accuracy laser-induced transient grating spectroscopy analysis method for probing near surface thermal diffusivity with gigahertz frequency instrumentation. *AIP Adv.* **14**, 105226, DOI: 10.1063/5.0196820 (2024).

19. Smith, R. J. *et al.* Spatially resolved acoustic spectroscopy for rapid imaging of material microstructure and grain orientation. *Meas. Sci. Technol.* **25**, 055902, DOI: 10.1088/0957-0233/25/5/055902 (2014).

20. Patel, R., Li, W., Smith, R. J., Sharples, S. D. & Clark, M. Orientation imaging of macro-sized polysilicon grains on wafers using spatially resolved acoustic spectroscopy. *Scripta Materialia* **140**, 67–70, DOI: 10.1016/j.scriptamat.2017.07.003 (2017).

21. Siegman, A. E. Bragg diffraction of a Gaussian beam by a crossed-Gaussian volume grating*. *J. Opt. Soc. Am.* **67**, 545–550, DOI: 10.1364/JOSA.67.000545 (1977).

22. Dennett, C. & Short, M. Time-resolved, dual heterodyne phase collection transient grating spectroscopy. *Appl. Phys. Lett.* **110**, DOI: 10.1063/1.4983716 (2017).

23. Sermeus, J., Sinha, R., Vanstreels, K., Vereecken, P. M. & Glorieux, C. Determination of elastic properties of a MnO2 coating by surface acoustic wave velocity dispersion analysis. *J. Appl. Phys.* **116**, 023503, DOI: 10.1063/1.4885427 (2014).

24. Hofmann, F. *et al.* Non-contact measurement of thermal diffusivity in ion-implanted nuclear materials. *Sci. Rep.* **5**, 1–7, DOI: 10.1038/srep16042 (2015).

25. Duncan, R. A. *et al.* Increase in elastic anisotropy of single crystal tungsten upon He-ion implantation measured with laser-generated surface acoustic waves. *Appl. Phys. Lett.* **109**, DOI: 10.1063/1.4964709 (2016).

26. Trachanas, E. *et al.* Thermal diffusivity variation assessment on Radio-Frequency Quadrupole Cu-OF copper due to proton irradiation. *Nucl. Instruments Methods Phys. Res. Sect. B: Beam Interactions with Mater. Atoms* **539**, 179–189, DOI: 10.1016/j.nimb.2023.04.002 (2023).

27. Reza, A. *et al.* Non-contact, non-destructive mapping of thermal diffusivity and surface acoustic wave speed using transient grating spectroscopy. *Rev. Sci. Instruments* **91**, 054902, DOI: 10.1063/5.0003742 (2020).

28. Zener, C. *Elasticity and Anelasticity of Metals* (University of Chicago Press, 1948).

29. Käding, O. W., Skurk, H., Maznev, A. A. & Matthias, E. Transient thermal gratings at surfaces for thermal characterization of bulk materials and thin films. *Appl. Phys. A Mater. Sci. Process.* **61**, 253–261, DOI: 10.1007/BF01538190 (1995).

30. Landa, M. *et al.* Modal resonant ultrasound spectroscopy for ferroelastics. *Appl. Phys. A* **96**, 557–567, DOI: 10.1007/s00339-008-5047-4 (2009).

31. Stoklasová, P., Sedlák, P., Seiner, H. & Landa, M. Forward and inverse problems for surface acoustic waves in anisotropic media: A Ritz-Rayleigh method based approach. *Ultrasonics* **56**, 381–9, DOI: 10.1016/j.ultras.2014.09.004 (2015).

32. Stoddart, P. R., Crowhurst, J. C., Every, A. G. & Comins, J. D. Measurement precision in surface Brillouin scattering. *J. Opt. Soc. Am. B* **15**, 2481, DOI: 10.1364/JOSAB.15.002481 (1998).

33. Every, A., Sumanya, C., Mathe, B., Zhang, X. & Comins, J. Optimized determination of elastic constants of crystals and their uncertainties from surface Brillouin scattering. *Ultrasonics* **69**, 273–278, DOI: 10.1016/j.ultras.2016.02.004 (2016).

34. Mañosa, L. & Planes, A. Materials with Giant Mechanocaloric Effects: Cooling by Strength. *Adv. Mater.* **29**, 1603607, DOI: 10.1002/adma.201603607 (2017).

35. Xiao, F., Bucsek, A., Jin, X., Porta, M. & Planes, A. Giant elastic response and ultra-stable elastocaloric effect in tweed textured Fe-Pd single crystals. *Acta Materialia* **223**, 117486, DOI: 10.1016/j.actamat.2021.117486 (2022).

36. Hou, H. *et al.* Fatigue-resistant high-performance elastocaloric materials made by additive manufacturing. *Science* **366**, 1116–1121, DOI: 10.1126/science.aax7616 (2019).

37. Tušek, J. *et al.* A regenerative elastocaloric heat pump. *Nat. Energy* **1**, 1–6, DOI: 10.1038/nenergy.2016.134 (2016).

38. Fähler, S. Caloric Effects in Ferroic Materials: New Concepts for Cooling. *Energy Technol.* **6**, 1394–1396, DOI: 10.1002/ente.201800201 (2018).

39. Bucsek, A. N., Nunn, W., Jalan, B. & James, R. D. Energy Conversion by Phase Transformation in the Small-Temperature-Difference Regime. *Annu. Rev. Mater. Res.* **50**, 283–318, DOI: 10.1146/annurev-matsci-082019-021824 (2020).

40. Lindquist, P., Chernenko, V., Cesari, E. & Müllner, P. Mechanical energy conversion to electricity through periodically stress-induced martensitic transformation in Co-Ni-Ga. *Scripta Materialia* **236**, 115667, DOI: 10.1016/j.scriptamat.2023.115667 (2023).

41. Faran, E. & Shilo, D. Ferromagnetic Shape Memory Alloys—Challenges, Applications, and Experimental Characterization. *Exp. Tech.* **40**, 1005–1031, DOI: 10.1007/s40799-016-0098-5 (2016).

42. Heczko, O., Seiner, H. & Fähler, S. Coupling between ferromagnetic and ferroelastic transitions and ordering in Heusler alloys produces new multifunctionality. *MRS Bull.* **47**, 618–627, DOI: 10.1557/s43577-022-00354-x (2022).

43. Glorieux, C. *et al.* On the character of acoustic waves at the interface between hard and soft solids and liquids. *The J. Acoust. Soc. Am.* **110**, 1299–1306, DOI: 10.1121/1.1396333 (2001).

44. Wolfe, J. P. *Imaging Phonons: Acoustic Wave Propagation in Solids* (Cambridge University Press, 1998).

45. Sugawara, Y., Wright, O. B. & Matsuda, O. Direct access to the dispersion relations of multiple anisotropic surface acoustic modes by Fourier image analysis. *Appl. Phys. Lett.* **83**, 1340–1342, DOI: 10.1063/1.1602151 (2003).

46. Tachizaki, T. *et al.* Scanning ultrafast Sagnac interferometry for imaging two-dimensional surface wave propagation. *Rev. Sci. Instruments* **77**, 043713, DOI: 10.1063/1.2194518 (2006).

47. Pluta, M., Every, A. G., Grill, W. & Kim, T. J. Fourier inversion of acoustic wave fields in anisotropic solids. *Phys. Rev. B* **67**, 094117, DOI: 10.1103/PhysRevB.67.094117 (2003).

48. Lamb, H. On the propagation of tremors over the surface of an elastic solid. *Philos. Trans. R. Soc. Lond.* **203**, 1–42 (1904).

49. Musgrave, M. J. P. *Crystal acoustics: introduction to the study of elastic waves and vibrations in crystals* (Holden-Day, San Francisco, 1970).

50. Song, Y. *et al.* A lightweight shape-memory alloy with superior temperature-fluctuation resistance. *Nature* **638**, 965–971, DOI: 10.1038/s41586-024-08583-7 (2025).

51. Repček, K. *et al.* Compliant Lattice Modulations Enable Anomalous Elasticity in Ni–Mn–Ga Martensite. *Adv. Mater.* 2406672, DOI: 10.1002/adma.202406672 (2024).

52. Verstraeten, B. *et al.* Determination of thermoelastic material properties by differential heterodyne detection of impulsive stimulated thermal scattering. *Photoacoustics* **3**, 64–77, DOI: 10.1016/j.pacs.2015.05.001 (2015).

53. Every, A. G. Supersonic surface acoustic waves on the 001 and 110 surfaces of cubic crystals. *J. Acoust. Soc. Am.* **138**, 2937–2944, DOI: 10.1121/1.4934557 (2015).

54. Kušnír, J. *et al.* Apparent anisotropic thermal diffusivity measured in cubic single crystals by transient grating spectroscopy. *J. Appl. Phys.* **133**, DOI: 10.1063/5.0136850 (2023).

55. Deng, J., Xu, Y., Guasch, O., Gao, N. & Tang, L. Nullspace technique for imposing constraints in the rayleigh–ritz method. *J. Sound Vib.* **527**, 116812, DOI: 10.1016/j.jsv.2022.116812 (2022).

56. Sedlák, P., Seiner, H., Zídek, J., Janovská, M. & Landa, M. Determination of all 21 independent elastic coefficients of generally anisotropic solids by resonant ultrasound spectroscopy: Benchmark examples. *Exp. Mech.* **54**, 1073–1085, DOI: 10.1007/s11340-014-9862-6 (2014).

57. Grabec, T., Sedlák, P. & Seiner, H. Application of the Ritz—Rayleigh method for Lamb waves in extremely anisotropic media. *Wave Motion* **96**, 102567, DOI: 10.1016/j.wavemoti.2020.102567 (2020).

Acknowledgments

This work has been financially supported by Czech Science Foundation [Project No. 22-13462S] and by the Operational Programme Johannes Amos Comenius of the Ministry of Education, Youth and Sport of the Czech Republic, within the frame of project Ferroic Multifunctionalities (FerrMion) [project No. CZ.02.01.01/00/22_008/0004591], co-funded by the European Union. The authors further acknowledge Dr. Miroslav Frost (Czech Acad. Sci.) for help with open data management.

Author contributions statement

All authors contributed equally to the work.

Competing interests

The authors declare no competing interests.

Data availability statement

The data that support the findings of this study (all UTGS maps and calculated Green's functions) have been uploaded to Zenodo repository with the identifier DOI: 10.5281/zenodo.16875359, and will be made open if the paper is accepted for publication. For reviewing/editorial purposes, the data can be accessed through: https://zenodo.org/records/16875359?preview=1&token=eyJhbGciOiJIUzUxMiIsImlhdCI6MTc1NTE3ODQ1OSwiZXhwIjoxNzY3MDUyNzk5fQ.eyJpZCI6IjhlOGFhNjk0LTU4OTgtNDM5Ny05YTBiLTViNTczN2I1MTIyNSIsImRhdGEiOnt9LCJyYW5kb20iOiIzYzg2NGRjZWVmZGM4MTY2ZjFmOWMxNTMxZWZhYWIwYSJ9.ZOzjhNZIlpdCP5DgHPLL77jRtv_tfc6tYKUkVam6AyMdbnVd_tWi96oKY6L6rSAa_7YP3URZwOHHiSWex8Q2_A.